Suppression of Hydrogen Embrittlement due to Local Partitioning of Hydrogen to Dispersed Intermetallic Compound Particles in Al-Zn-Mg-Cu Alloys

Fujihara, Hiro
Department of Mechanical Engineering, Kyushu University

Shimizu, Kazuyuki
Department of Physical Science and Materials Engineering, Iwate University

Toda, Hiroyuki
Department of Mechanical Engineering, Kyushu University

Takeuchi, Akihisa
Japan Synchrotron Radiation Research Institute

他

出版情報：Materials transactions. 63 (10), pp.1406-1415, 2022-09-25. 公益社団法人日本金属学会
バージョン：

Materials Transactions, Vol. 63, No. 10 (2022) pp. 1406 to 1415

Suppression of Hydrogen Embrittlement due to Local Partitioning of Hydrogen to Dispersed Intermetallic Compound Particles in Al–Zn–Mg–Cu Alloys

Hiro Fujihara[1,*], Kazuyuki Shimizu[2], Hiroyuki Toda[1], Akihisa Takeuchi[3] and Masayuki Uesugi[3]

[1]*Department of Mechanical Engineering, Kyushu University, Fukuoka 819-0395, Japan*
[2]*Department of Physical Science and Materials Engineering, Iwate University, Iwate 020-0061, Japan*
[3]*Japan Synchrotron Radiation Research Institute, Hyogo 679-5198, Japan*

Recent studies have revealed that hydrogen embrittlement in Al–Zn–Mg alloys appears to be dominated by hydrogen partitioning to $MgZn_2$ precipitates. A method has recently been proposed for reducing the hydrogen concentration at $MgZn_2$ precipitates by adding specific intermetallic compound particles that have high hydrogen trap energy. In the present study, the effectiveness of Al_7Cu_2Fe particles on suppression of hydrogen embrittlement in Al–Zn–Mg–Cu alloys was evaluated using X-ray microtomography. Quasi-cleavage cracks were found to be initiated in regions where local volume fractions of the Al_7Cu_2Fe particles were relatively low. Hydrogen partitioning to the $MgZn_2$ precipitate interface was suppressed, even in high hydrogen concentration material, by adding Al_7Cu_2Fe particles. However, the fractional area of the quasi-cleavage fracture in the material with high hydrogen concentration was higher due to insufficient hydrogen diffusion inside the Al_7Cu_2Fe particles and at the interface between the aluminum matrix and the particles. It appears that finely distributed small Al_7Cu_2Fe particles might effectively suppress hydrogen embrittlement. [doi:10.2320/matertrans.MT-L2022007]

(Received March 28, 2022; Accepted July 9, 2022; Published September 25, 2022)

Keywords: *Al–Zn–Mg alloy, hydrogen embrittlement, hydrogen partition, intermetallic compound particle, X-ray microtomography*

1. Introduction

Hydrogen in metallic materials degrades their mechanical properties. This phenomenon is called hydrogen embrittlement (HE).[1,2] In high-strength Al–Zn–Mg alloys, intergranular and quasi-cleavage fractures appear as HE fractures.[3–5] To suppress HE, several methods have been proposed and applied.[6–8] Among them, over-aging treatment is widely employed in Al–Zn–Mg alloy but causes reduction in strength.[6,7] An alternative method for HE suppression without causing loss of strength is retrogression-reaging (RRA) treatment.[7,8] At grain boundaries, precipitates are coarsened by RRA treatment, which results in HE suppression.[8,9] Even by employing RRA treatment, HE suppression cannot be ensured due to the scattering of the size distribution of grain boundary precipitates.[10] Reducing the hydrogen concentration in a material also leads to HE suppression.[11,12] However, to prepare a material with low hydrogen concentration, fabrication and thermal treatments must be performed under high vacuum conditions that are commercially not viable.[12]

Recently, Tsuru *et al.* revealed that the $MgZn_2$ precipitate interface spontaneously debonds as a result of hydrogen accumulation, and proposed this as a new mechanism for quasi-cleavage fracture in Al–Zn–Mg alloys.[13] It can be inferred that quasi-cleavage fracture is suppressed by reducing the hydrogen concentration at the $MgZn_2$ precipitate interface. To control hydrogen concentration at the $MgZn_2$ precipitate interface, hydrogen partitioning behavior should be quantitatively understood. Hydrogen partitioning behavior can be calculated by assuming that hydrogen atoms trapped at interstitial lattice sites and at other trap sites are in a state of local equilibrium as follows:[14]

$$\frac{\theta_i}{1-\theta_i} = \theta_{\mathrm{L}} \exp\left(\frac{E_{\mathrm{b},i}}{RT}\right) \tag{1}$$

where θ_L is the hydrogen occupancy of the interstitial lattice site, θ_i is the occupancy of the i^{th} trap site, and $E_{\mathrm{b},i}$ is the hydrogen trap energy of the i^{th} trap site. The total hydrogen concentration is expressed as the sum of the hydrogen concentration, C_{H}, at all trap sites as follows:[15,16]

$$C_{\mathrm{H}} = \theta_L N_L + \sum \theta_i N_i + C_{\mathrm{pore}} \tag{2}$$

where N_L and N_i are the trap site densities in the interstitial lattice site and the i^{th} trap site. C_{Pore} is the hydrogen concentration in the micropores. According to the above equations, hydrogen is partitioned in accordance with the trap site density and the trap energy of each trap site. Hydrogen concentration at the $MgZn_2$ precipitate interface can be suppressed by increasing the number of trap sites that have a higher hydrogen trap energy than the $MgZn_2$ precipitate interface, without reducing the hydrogen concentration in the material.

A recent study using first-principles calculation by Yamaguchi *et al.* revealed that Al_7Cu_2Fe particles in Al–Zn–Mg alloys[17,18] have hydrogen trap energy of 54.0 kJ/mol which is slightly higher than that of $MgZn_2$ precipitate (53.8 kJ/mol).[19] It has been experimentally confirmed that hydrogen is trapped in the Al_7Cu_2Fe interior.[20] According to Su *et al.*,[21] the fractional area of quasi-cleavage fractures in Al–Zn–Mg–Cu alloy is reduced by increasing the amount of Al_7Cu_2Fe particles. Figure 1 shows a summary of the relationships among quasi-cleavage fracture, volume fraction of Al_7Cu_2Fe particles, and hydrogen concentration at the Al_7Cu_2Fe particles and the $MgZn_2$ precipitate.[19,21] It can be seen that reduction of the fractional area of the quasi-cleavage fracture is correlated with reducing hydrogen concentration at the $MgZn_2$ precipitate interface with increasing the volume fraction of the Al_7Cu_2Fe particles. Using this method, HE can

*Corresponding author, E-mail: fujihara@mech.kyushu-u.ac.jp

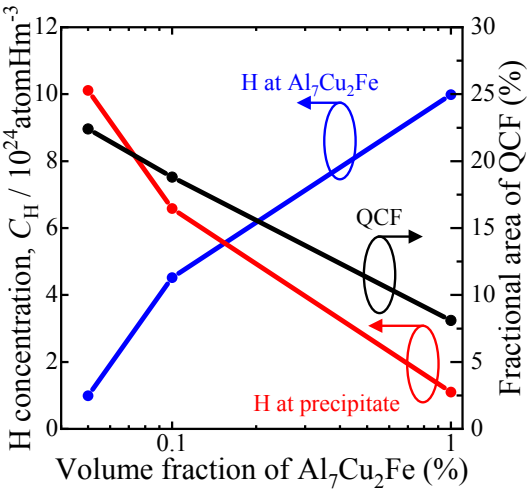

Fig. 1 Effects of Al_7Cu_2Fe particle addition on hydrogen partitioning to $MgZn_2$ precipitates, and the quasi-cleavage fracture (QCF).[19,21]

be suppressed with no need for any of the special HE suppression methods discussed above.

To utilize this method practically, it is necessary to quantitatively analyze the conditions for HE suppression assuming actual use. Regions of extremely high hydrogen concentration are locally formed, for example by corrosion.[22,23] In high hydrogen concentration regions such as these, hydrogen partitioning to the $MgZn_2$ precipitate interface and associated HE may not be suppressed, for example, due to the trapping of limited hydrogen in the Al_7Cu_2Fe particles. The distribution of the Al_7Cu_2Fe particles also affects HE behavior. Wang *et al.* reported that hydrogen partition to the $MgZn_2$ precipitate is not suppressed in regions where Al_7Cu_2Fe particles are not present.[24] It is therefore necessary to investigate the effects of HE suppression by intermetallic compound (IMC) particles using different volume fractions and various hydrogen concentrations. In the present study, four-dimensional (i.e., time axis and Euclidean space) observation of HE behavior was performed in two Al–Zn–Mg alloys in which the hydrogen concentration and the particle density had been varied. To investigate specific conditions of HE suppression methods, we evaluated the influence of hydrogen concentration and the distribution of the Al_7Cu_2Fe particles on the initiation and propagation behavior of local HE cracks.

2. Experimental Procedure

2.1 Materials

Two Al–10Zn–2.4Mg–1.5Cu (mass%) alloys with different Fe and Si content were prepared. The chemical compositions are summarized in Table 1. The alloys with high and low amounts of Fe and Si are called HFeSi and LFeSi, respectively. Figure 2 shows two preparation processes of the materials with low and high hydrogen concentrations (herein LH and HH materials, respectively). The ingots were heated at a rate of 50 K/min up to 773 K, homogenized at this temperature for 1440 min and then hot-rolled with a rolling reduction of 74% at 673 K. To produce the LH and HH materials, two types of treatments were applied to both materials after hot rolling. For LH materials, to vary the hydrogen concentration, the thermal cycle process was performed under a vacuum of 5×10^{-4} Pa. The temperature range of the thermal cycle was 300–633 K, the heating rate was 1.7 K/min, and the number of cycles was set to 2. According to Oikawa *et al.*, who observed microstructures after the same thermal cycling process for the same materials, grain size and structure were not changed by the present thermal cycling process.[25] Solution treatment at 748 K for 120 min was then conducted, also in a vacuum. In contrast, for HH materials, after hot-rolling, solution treatment in air was conducted. Immediately after the solution treatment, both materials were aged at 300 K for 5760 min, at 393 K for 360 min, and finally at 423 K for 300 min.

The gauge length and cross-sectional area of the specimen for the *in-situ* tensile tests were 0.7 mm and 0.6 mm × 0.6 mm, respectively; the same dimensions as in the previous report.[21] All specimens were machined so that the tensile load was applied in the rolling direction. Hydrogen was charged into HH materials using electrical discharge machining (EDM) in water, as in previous report.[11] To prepare the specimen with extremely high hydrogen concentration, first, HH materials were cut into plate-like form with a thickness of 0.8 mm. Next, 0.05 mm was cut out from both sides of the plate surface. Cutting twice in this way results in a final thickness of 0.6 mm. An interval of 1440 min was maintained between the two cuttings so as to distribute the charged hydrogen to the specimen interior.[26] Finally, the specimen for the *in-situ* tensile test was cut out from the plate by EDM in water. In contrast, LH materials were prepared by EDM in oil to suppress hydrogen charging during EDM. The four types of materials, which were prepared using the above processes, are respectively called HFeSi-HH, HFeSi-LH, LFeSi-HH, and LFeSi-LH materials.

The total hydrogen concentration in each material were measured using a gas chromatography-type thermal desorption analyzer (PDHA-1000, Nissha FIS, Inc.). The thermal desorption experiment was performed by heating from room temperature to 773 K at a heating rate of 1.5 K/min. High purity (6N) argon carrier gas was passed through a quartz tube at a flow rate of 20 mL/min. Figure 3 shows the thermal desorption curves obtained from all the materials. The

Table 1 Chemical compositions of the two alloys used (mass%).

	Si	Fe	Cu	Mg	Zn	Ti	Zr	Al
HFeSi	0.30	0.30	1.5	2.4	10.0	0.04	0.15	Bal.
LFeSi	0.01	0.01	1.5	2.4	10.0	0.04	0.15	Bal.

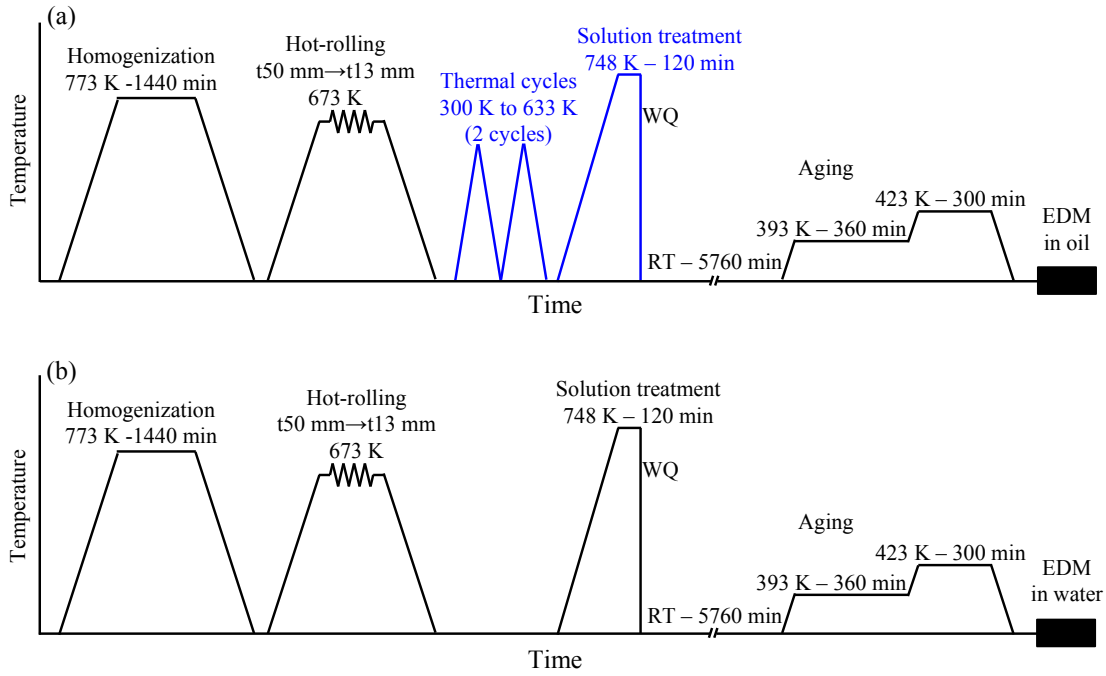

Fig. 2 Schematic diagrams of the processes used to prepare (a) low hydrogen concentration and (b) high hydrogen concentration materials. The processes performed under vacuum are indicated in blue.

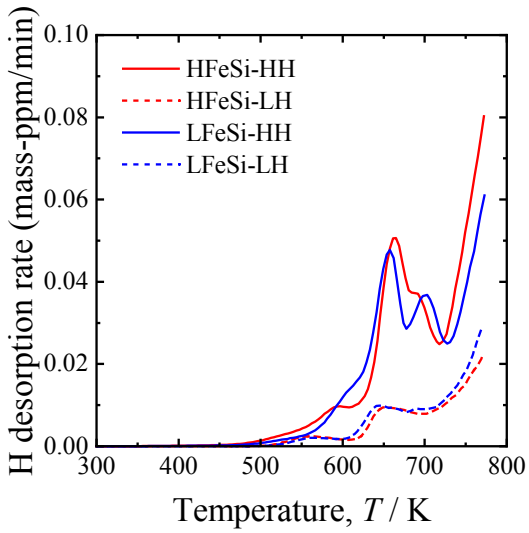

Fig. 3 Thermal desorption curves of hydrogen for each material. Heating rate was 1.5 K/min. The solid lines and dotted lines were obtained from HH and LH materials, respectively.

cumulative hydrogen concentrations from room temperature to 773 K in each material were respectively 5.4, 2.4, 5.7, and 2.1 mass ppm in HFeSi-HH, HFeSi-LH, LFeSi-HH, and LFeSi-LH materials.

2.2 *In-situ* tensile test and measurement of 3D image-based analysis

An *in-situ* tensile test for each specimen using X-ray microtomography (herein called XMT) was performed at BL20XU beamline in SPring-8, Japan. A monochromatic X-ray beam with an energy of 20 keV was used. The image detector was a 2048 × 2048 pixel element digital CMOS camera. The distance from the specimen to the image detector was 20 mm. A total of 1800 images were captured in 0.1° increments over a range of 180°. The pixel size of the image detectors was 0.5 µm. Scans were performed while holding an applied strain for 55.6 min at each tensile step.

3D images were reconstructed using a convolution back-projection algorithm. A linear absorption coefficient of −30 to 40 cm^{-1} was collected to fit the 8-bit grayscale from 0 to 255 as in the previous report.[21] The Marching Cubes algorithm was used to calculate the gravity center, volume, surface area, and equivalent diameter of the Al_7Cu_2Fe particles in each specimen.[27] To eliminate the inaccuracies generated from image noise, only Al_7Cu_2Fe particles over 9 voxels in volume were counted. Figure 4 shows virtual cross-sections of 3D reconstructed images prior to the deformation. The tensile load was applied in the rolling direction. Volume fractions of the Al_7Cu_2Fe particles were 1.19%, 1.40%, 0.09%, and 0.36% in HFeSi-HH, HFeSi-LH, LFeSi-HH, and LFeSi-LH materials, respectively. In the present study, the same materials (same lot and same ingot) were used to prepare LFeSi and HFeSi materials. The error in volume fraction of the Al_7Cu_2Fe particle in LFeSi materials could be from scattering of the distribution of the Al_7Cu_2Fe particles. To measure the distribution of 3D plastic strain, the microstructural tracking technique was applied by tracking all the Al_7Cu_2Fe particles throughout the deformation.[28] High-density 3D plastic strain mapping was also achieved by calculating the physical displacement of identical particles.[28]

2.3 Hydrogen partitioning behavior

The hydrogen occupancy of each trap site can be calculated using eq. (1) and (2). The calculation of hydrogen concentration in the micropores, C_{Pore}, is detailed in the previous reports.[29,30] Hydrogen trap behavior of lattice defects, precipitates and IMC particles in the aluminum

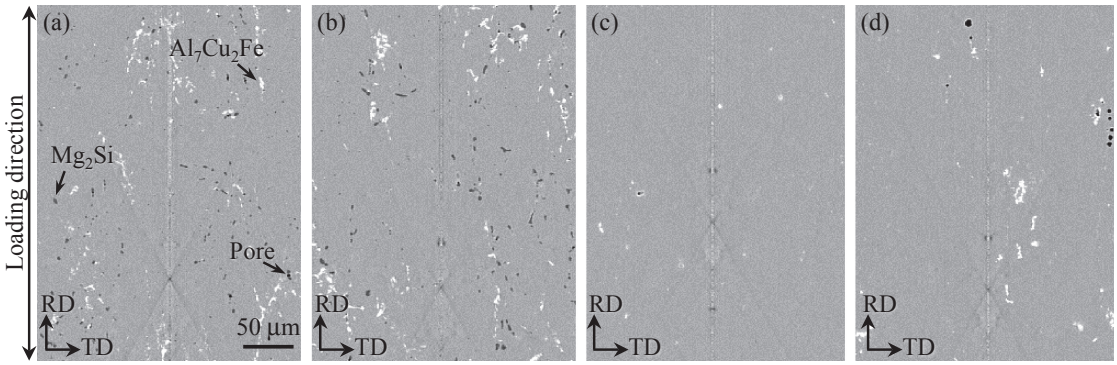

Fig. 4 Virtual cross-sections captured by X-ray microtomography showing typical distributions of micropores (black), Mg_2Si particles (gray) and Al_7Cu_2Fe particles (white) in each material; (a) HFeSi-HH, (b) HFeSi-LH, (c) LFeSi-HH, and (d) LFeSi-LH.

alloys was studied using first-principles calculations.[19,30–36] They revealed the major hydrogen trap sites in the Al–Zn–Mg alloys to be solute Mg atoms, vacancies, dislocations, grain boundaries, precipitate interfaces, Al_7Cu_2Fe particles, and micropores.[19,30–36] Mg_2Si particles and Al_3Zr precipitates were distributed in the alloys used in the present study. Yamaguchi *et al.* and Xu *et al.*, who studied hydrogen trap behavior of Mg_2Si particles and Al_3Zr precipitates using first-principles calculations, revealed that they act as hydrogen trap sites.[24,37,38] However, the amount of hydrogen trapped at these trap sites is quite low due to the low trap site density or hydrogen trap energy.[24,37,38] The present analysis did not take into account the influence of Mg_2Si particles and Al_3Zr precipitates, since it is the influence of these trap sites on hydrogen partitioning behavior appears to be negligible. Hydrogen is partitioned according to the trap site density and the trap energy of each trap site. The hydrogen trap energies have been analyzed using first-principles calculations, and are summarized in Table 2.[19,30–36] To estimate the trap site densities of each trap site, the number of solute Mg atoms, vacancy concentration, dislocation density, volume fraction of Al_7Cu_2Fe particles, and surface areas of precipitates and micropores were calculated. The distribution of vacancy concentration and dislocation density that is increased by deformation was calculated using the 3D equivalent plastic strain distribution referred to in the previous reports.[16,21] The fractional area of grain boundaries was calculated from the average grain size which was measured in the previous report[12] using an optical microscope. The fractional area of the precipitate interface was obtained via transmission electron microscopy (TEM).[39,40] The volume of Al_7Cu_2Fe particles and surface area of micropores were measured using a reconstructed 3D image obtained in the XMT experiment. Details of the quantification of the trap site densities are available elsewhere.[13,16,21,41]

Table 2 Summary of the hydrogen trap energies derived using first-principles calculations.[19,30–36]

Trap site	Binding energy, E_b (kJ/mol)	Ref.
Edge dislocation	7.7	31
Solute Mg atom	11.6	32
Screw dislocation	16.4	31
Grain boundary	19.3	33
Vacancy	28.9	34
Precipitate (Coherent interface)	8.6-32.6	35
Precipitate (Semi-coherent)	53.8	36
Al_7Cu_2Fe particle (Inside)	54.0	19
Pore surface	67.5	30

The number of hydrogen atoms that a trap site can trap per unit number, unit length, unit area, and unit volume (herein called the hydrogen trap interval) has been reported using first-principles calculations.[13,19,30–36] The reported hydrogen trap intervals are 1.0 atomH/atom for the solute Mg atoms,[32] 1.0 atomH/nm for the edge dislocation,[31] 1.2 atomH/nm for the screw dislocation,[31] 8 atomH/vacancy for the vacancy,[34] 21.9 atomH/nm^2 for the grain boundary,[33] 17.1 atomH/nm^2 for the coherent interface of the $MgZn_2$ precipitate,[13,35] 5.6 atomH/nm^2 for the semi-coherent interface the $MgZn_2$ precipitate,[36] 13.2 atomH/nm^3 for the Al_7Cu_2Fe particle,[19] and also 20 atomH/nm^2 for the micropore.[30]

3. Experimental Results

3.1 Macroscopic fracture behavior

Figures 5 and 6 respectively show the nominal stress-strain responses and the fracture surfaces. The results of *in-situ* tensile test are summarized in Table 3. With increasing IMC particle content, the strain at which cracks initiated decreased by 60–78% and fracture strain decreased by 17–58%. The fractured strain decreases due to the presence of brittle IMC particles. With increasing hydrogen concentration, the strain at which crack initiate decreased by 45–69%, and fracture strain decreased by 54–74%. Reduction in crack initiation and fracture strain with hydrogen concentration is due to the difference in hydrogen concentration at the $MgZn_2$ precipitate interface. Fracture surfaces of all materials are composed of quasi-cleavage and ductile fractures. All quasi-cleavage cracks initiated near the specimen surface and then gradually propagated towards the center of the specimens. Fractional areas of quasi-cleavage fracture, which are framed in yellow in Fig. 6, increased with increasing hydrogen concentration. It can be inferred that hydrogen charging enhanced the

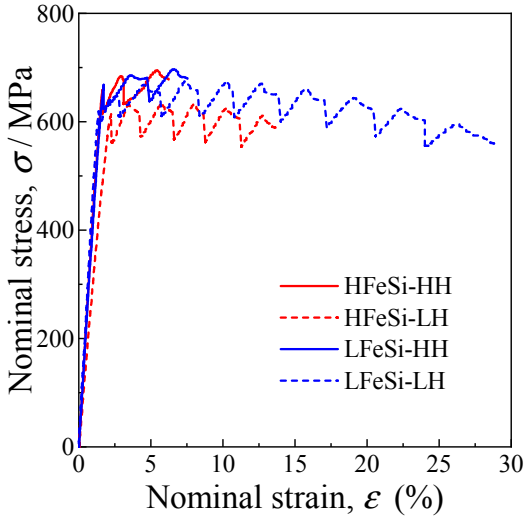

Fig. 5 Nominal stress-strain responses obtained by the *in-situ* tensile tests.

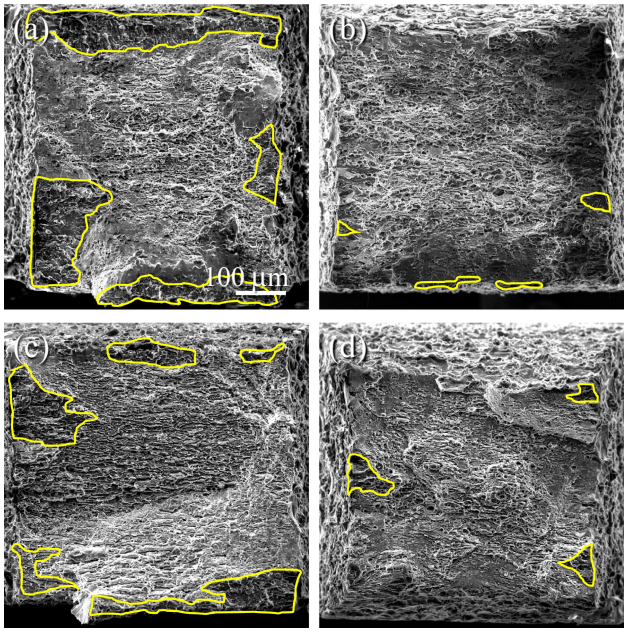

Fig. 6 Fracture surfaces after the *in-situ* tensile tests; (a) HFeSi-HH, (b) HFeSi-LH, (c) LFeSi-HH, and (d) LFeSi-LH. The quasi-cleavage crack regions are indicated in yellow solid lines.

initiation and propagation of quasi-cleavage cracks, eventually leading to ductility loss. An inverse relationship was found between amounts of Fe and Si and the fractional area of quasi-cleavage fracture in HH and LH materials. The

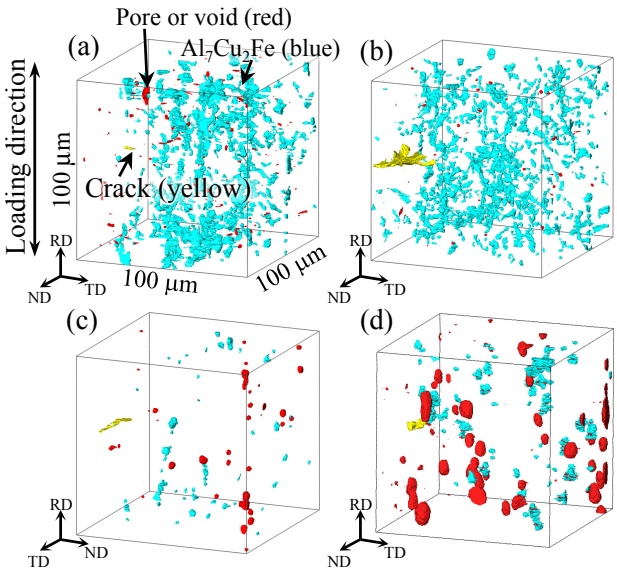

Fig. 7 3D observation of the quasi-cleavage cracks in (a) HFeSi-HH at applied strain $\varepsilon_{appl} = 3.1\%$, (b) HFeSi-LH at $\varepsilon_{appl} = 4.3\%$, (c) LFeSi-HH at $\varepsilon_{appl} = 1.7\%$, and (d) LFeSi-LH at $\varepsilon_{appl} = 14.0\%$. Micropores and voids are shown in red. Al_7Cu_2Fe particles and cracks are indicated in blue and yellow, respectively.

difference in the fractional area of quasi-cleavage fracture between HFeSi-LH and LFeSi-LH materials was small (1%), and it can be expected that the opposite trend may be found if the microstructure is slightly different. Although the same material (same lot and same ingot) was used in the present study, the microstructure differs slightly according to cutting location. It can be inferred that the slight difference in the microstructure in each specimen led to the opposite trend in HH and LH materials.

3.2 HE crack initiation and propagation behavior

The strains at which cracks initiate decreased with increasing hydrogen concentration, as summarized in Table 3. In LH materials, cracks were initiated after the maximum stress. The influence of the local distribution of Al_7Cu_2Fe particles on crack initiation was evaluated. Figure 7 shows the 3D distribution of Al_7Cu_2Fe particles and micropores around the initiated quasi-cleavage crack in each material. The volume fraction, V_f, and mean equivalent diameter, d_m, of Al_7Cu_2Fe particles in both the whole specimen and the local region ahead of the crack tip associated with Figs. 7 are summarized in Table 4. The volume fraction in these local regions, $V_{f,local}$, was 3.1–12.7 times less than in the whole specimen, $V_{f,whole}$. Cracks

Table 3 Summary of results from the *in-situ* tensile tests of each material.

	HFeSi-HH	HFeSi-LH	LFeSi-HH	LFeSi-LH
Strain at which crack initiate (%)	3.1	4.3	1.7	14.0
Fracture strain (%)	6.2	13.6	7.5	28.8
Fractional area of QCF (%)	25	2	19	3

Table 4 Results of 3D image analysis of Al_7Cu_2Fe particles showing their mean equivalent diameter in the whole specimen, $d_{m,\,whole}$, their volume fraction in the whole specimen, $V_{f,\,whole}$, and ahead of the crack tip, $V_{f,\,local}$.

	HFeSi-HH	HFeSi-LH	LFeSi-HH	LFeSi-LH
$d_{m,\,whole}$ (μm)	3.2	3.7	2.8	3.7
$V_{f,\,whole}$ (%)	1.19	1.40	0.09	0.36
$V_{f,\,local}$ (%)	0.38	0.11	0.01	0.04
$V_{f,\,whole}$ / $V_{f,\,local}$	3.1	12.7	9.0	9.0

initiated in local regions where the Al_7Cu_2Fe particles were sparsely distributed.

To investigate the influence of the Al_7Cu_2Fe particles on the propagation behavior of quasi-cleavage cracks, local hydrogen partitioning behavior ahead of the crack tip was evaluated. The plastic strain distribution was measured to calculate increments of vacancy concentration and dislocation density during deformation. Figure 8 shows the equivalent plastic strain distributions in regions where quasi-cleavage cracks propagated. The ranges of calculated applied strain were from no loading to the step at which a crack initiated. In LH materials, the equivalent strain was localized at the center of the specimens, caused by necking. The equivalent strain in HH materials was lower than that in LH materials because the cracks were initiated before necking in HH materials.

The local hydrogen partitioning behavior ahead of the crack tips in each material was analyzed according to eqs. (1) and (2). The increment in vacancy concentration and dislocation density by deformation was calculated using the equivalent plastic strain distribution. Figures 9(a) and (b) show the hydrogen concentration and occupancy of each trap site, respectively, in each material. The sum of hydrogen atoms trapped at the Al_7Cu_2Fe particles, semi-coherent interfaces of the $MgZn_2$ precipitates, and micropores is more than 99.8% in all the materials, as shown in Fig. 9(a). Shimizu *et al.*, who assessed the hydrogen trapping and partitioning behavior at the interface of the $MgZn_2$ precipitate, reported the hydrogen concentration at the precipitate interface to be more than 90% of the total concentration in materials without IMC particles.[36] In the present study, the hydrogen concentration at the precipitate interface was approximately 80% of the total concentration, even for LFeSi-HH material, which has the highest hydrogen concentration at the precipitates. Hydrogen concentrations at each trap site correspond to the hydrogen trap energy of each trap site.[14,15] Since the trap energies of the $MgZn_2$ precipitate (i.e., 53.8 kJ/mol) and the Al_7Cu_2Fe particles (i.e., 54.0 kJ/mol) are approximately the same, and hydrogen partitioning to the $MgZn_2$ precipitate is suppressed, even in the presence of a single particle. In the analyzed region ahead of the crack tip in LFeSi-HH material, there was single Al_7Cu_2Fe particle, and hydrogen partitioning to the $MgZn_2$ precipitate was suppressed.

The suppression of hydrogen partitioning to the $MgZn_2$ precipitate was stronger in HFeSi material than in LFeSi material because the decreasing value of hydrogen concentration is a function of the local trap site density (i.e., volume fraction) of the particles. The hydrogen concentration and occupancy of the precipitate interface in HFeSi-HH material decreased to mid-level between LFeSi-HH material and LH materials, as shown in Fig. 9. The relationship between quasi-cleavage fracture and the hydrogen occupancy of the semi-coherent interface of the $MgZn_2$ precipitate is summarized in Fig. 10. It was found that the fractional area of the quasi-cleavage fracture decreased with decreasing hydrogen occupancy of the $MgZn_2$ precipitate interface. However, the fractional area of quasi-cleavage fracture of HFeSi-HH material was deviated from this trend and showed a maximum value despite having similar hydrogen occupancy of the $MgZn_2$ precipitate to LH materials. The inverse relationship was found: that a relationship between the amount of Fe and Si and the fractional area of quasi-cleavage fracture between HH and LH materials could be caused by a slight difference in the microstructure in each specimen, as described in Section 3.1.

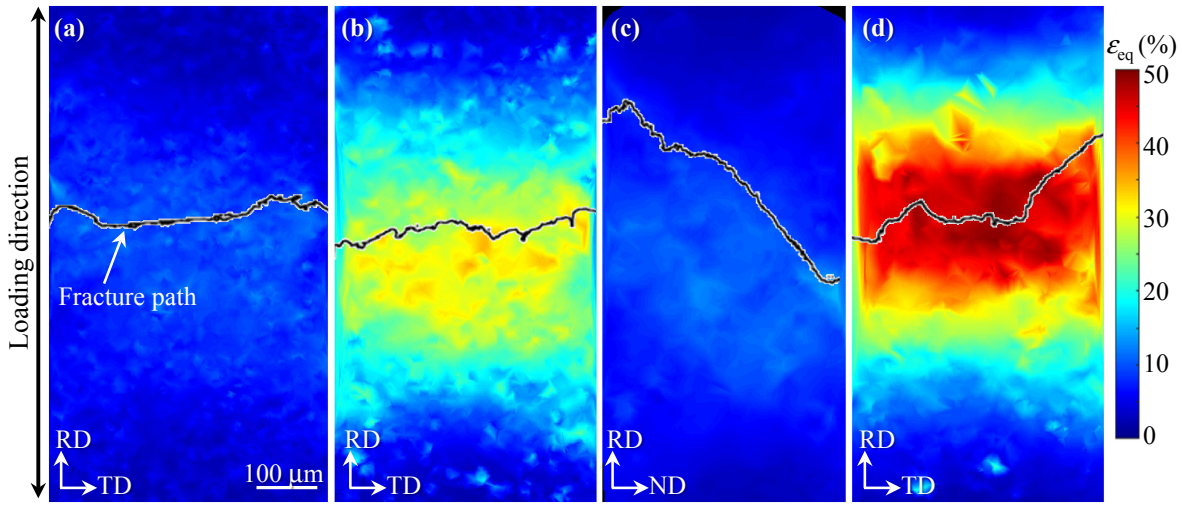

Fig. 8 3D equivalent strain, ε_{eq}, distribution, calculated from ε_{appl} of 0 to (a) 3.1% in HFeSi-HH, (b) 4.3% in HFeSi-LH, (c) 1.7% in LFeSi-HH, and (d) 14.0% in LFeSi-LH. The fracture paths are shown as black lines.

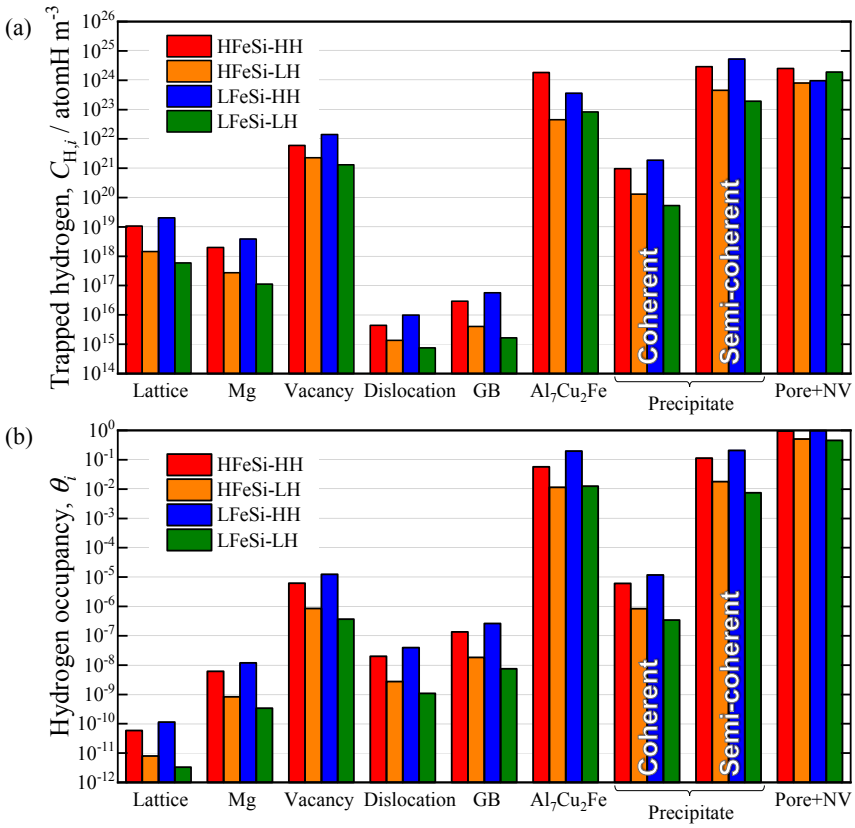

Fig. 9 Summary of the hydrogen partitioning behavior in each material: (a) hydrogen concentration and (b) hydrogen occupancy in each trap site.

4. Discussion

4.1 Influence of hydrogen and particles on crack initiation

The quasi-cleavage cracks in HH materials were initiated earlier than those in LH materials. According to Tsuru *et al.*, the interfacial cohesive energy of the $MgZn_2$ precipitate interface decreases with increasing in hydrogen concentration at the interface.[13] Based on this report, the interfacial cohesive energy in HH materials was less than that in LH materials, and the interface may debond earlier in HH materials. Eventually, nano-cracks associated with debonded precipitate interfaces coalesce, which could finally enhance quasi-cleavage crack initiation in HH materials.

Osaki *et al.* reported the initiation of hydrogen-induced transgranular cracks to be associated with microcracks initiated at the interface between the Al_7Cu_2Fe particles and the aluminum matrix.[42] Based on this report, it might be expected that the number of cracks at the surface would increase with an increased number of particles. However, as shown in Fig. 6, there is no clear change in the number of quasi-cleavage cracks and the crack-initiated region around the surface between HFeSi and LFeSi materials. On the other hand, according to the crack initiation mechanism proposed by Tsuru[13] and local thermal equilibrium relationship (eq. (1)),[14] hydrogen partitioning to the $MgZn_2$ precipitate and associated HE behavior is promoted by a decrease in the number of Al_7Cu_2Fe particles. Wang *et al.* showed that hydrogen partitioning to the $MgZn_2$ precipitate interface could not be suppressed in regions where the spatial distribution of the Al_7Cu_2Fe particles was sparse.[24] In the present study also, it was found that quasi-cleavage crack initiated in the region in which the Al_7Cu_2Fe particles were sparsely distributed, even if the number of Al_7Cu_2Fe particles was high throughout the specimen. It can be inferred that the strain at which the cracks initiated varied due to a difference in hydrogen partitioning to the $MgZn_2$ precipitate interface caused by the difference in hydrogen concentration and 3D local particle distribution, rather than by the presence of particles at the specimen surface. It can therefore be expected that finely distributed Al_7Cu_2Fe particles in 3D can significantly suppress hydrogen partitioning to $MgZn_2$ and associated quasi-cleavage crack initiation.

4.2 Influence of hydrogen and particles on crack propagation

Osaki *et al.* indicated that surface microcracks initiated at the interface between particles and the aluminum matrix propagate as transgranular cracks, following the hydrogen-enhanced localized plasticity (HELP) mechanism.[42] According to this report, HE cracks propagation might not be suppressed in spite of Al_7Cu_2Fe particles, which have high hydrogen trap energy, being present in the vicinity of crack tip. In the present study also, the fractional area of quasi-cleavage fracture in HFeSi-HH material was not suppressed despite the suppressed hydrogen occupancy of the $MgZn_2$ precipitate, as shown in Fig. 10. Only eq. (1) is used to calculate hydrogen partitioning behavior in a thermal equilibrium relationship between the interstitial site and a trap site. It can be inferred that one of the reasons why the

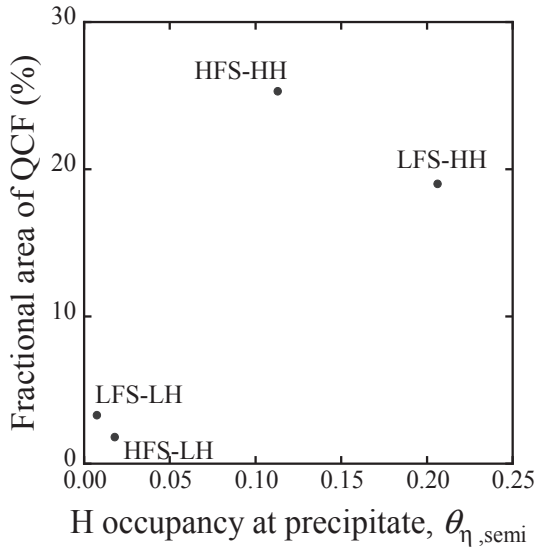

Fig. 10 Relationship between fractional area of QCF and hydrogen occupancy at the semi-coherent interface of the $MgZn_2$ precipitate.

quasi-cleavage fracture is not suppressed in HFeSi-HH material is that a thermal equilibrium relationship between the interstitial sites and Al_7Cu_2Fe particles was not achieved. While load is kept applied, hydrogen accumulates around the crack tip, where hydrostatic stress is concentrated.[43] The authors found the quasi-cleavage cracks propagated in such hydrogen-accumulated region ahead of the crack tip by multimodal image-based simulation combined with the crystal plasticity finite element method and hydrogen diffusion analysis.[44] $MgZn_2$ precipitates trap hydrogen at its interface, according to Tsuru *et al.*[35] The precipitates can immediately trap accumulated hydrogen. On the other hand, the Al_7Cu_2Fe particles can trap hydrogen in their interior, according to Yamaguchi.[19] Figures 11(a) and (b) illustrate the schematic diagrams of hydrogen distribution in the thermal equilibrium state and the non thermal equilibrium state, respectively, in the regions where hydrogen accumulated. Hydrogen must be sufficiently diffused to the particle interior at thermal equilibrium, as shown in Fig. 11(a). Accumulated hydrogen can diffuse to the particle interior via two processes: (i) passing through the matrix/particle interface and (ii) diffusion within the particle interior.

First, the effect of matrix/particle interface (process (i)) was considered. Chan *et al.*, who investigated hydrogen diffusion behavior in a martensitic steel, reported that the hydrogen diffusivity was slowed by hydrogen trapping behavior at the interface between martensite and austenite.[45] According to Oriani,[14] hydrogen diffusivity is reduced if a hydrogen trap site is present on the diffusion path. It was reported that the interface between the matrix and IMC particles has extremely high hydrogen trapping energy However, the amount of hydrogen trapped at these trap sites is quite low due to the low trap site density or hydrogen trap energy.[24,37,46,47] The interface of the Al_7Cu_2Fe particles may also strongly traps hydrogen. Hydrogen diffusion into the interior of the Al_7Cu_2Fe particles is likely delayed by the presence of strong trap sites on the diffusion path from the matrix into the interior of the Al_7Cu_2Fe particles.

Second, the effect of hydrogen diffusion behavior in the particle (process (ii)) was considered. From the displacement holding time (55.6 min) during tensile testing and the mean equivalent diameters of the particles (2.8–3.7 μm), as listed in Table 4, the diffusivity required for sufficient diffusion to the particle interior was higher than 1×10^{-15} m^2/sec. There are reports on hydrogen diffusivity in intermetallic compounds.[48,49] For example, at room temperature (300 K), the hydrogen diffusivity inside Mg_2NiH_4 and Al_2O_3 are reported to be 2.9×10^{-17} m^2/sec[48] and 2.1×10^{-15} m^2/sec,[49] respectively. If the hydrogen diffusivity inside the Al_7Cu_2Fe particles at room temperature is similar to that in Mg_2NiH_4 (2.9×10^{-17} m^2/sec),[48] hydrogen cannot sufficiently diffuse to the particle interior, as shown in Fig. 11(b). When the trap site density was estimated in terms of the volume of particles into which hydrogen could diffuse, it was approximately 27% of the total trap site density. Approximately 73% of the hydrogen concentration in the Al_7Cu_2Fe particles shown in Fig. 9(a) may be partitioned to the sites other than the particles. Based on the relationship of trap energies of each trap site, most of such hydrogen is likely partitioned to the $MgZn_2$ precipitate interfaces.[14,15] It was inferred that hydrogen partitioning to the $MgZn_2$ precipitate could not be

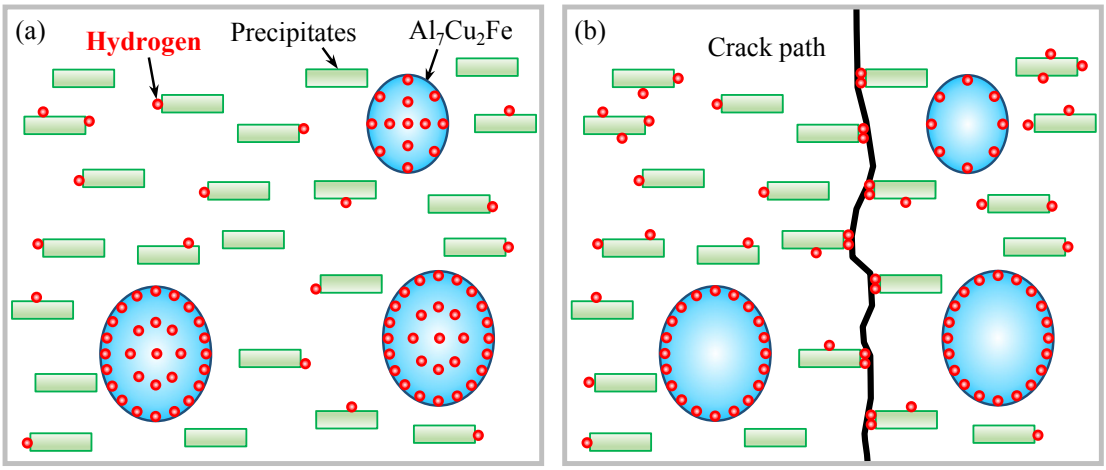

Fig. 11 Schematic illustration of the effect of Al_7Cu_2Fe particles on the suppression of hydrogen embrittlement in the regions where hydrogen accumulated. (a) thermal equilibrium and (b) non thermal equilibrium states.

suppressed because the particles could not sufficiently trap the accumulated hydrogen at the crack tip. On the other hand, if the hydrogen diffusivity inside the Al_7Cu_2Fe particles at room temperature is similar to that of Al_2O_3 (2.1×10^{-15} m^2/sec), hydrogen can be sufficiently diffused to the particle interior, resulting in HE suppression. Since HE was not suppressed in HFeSi-HH material, it was expected that the Al_7Cu_2Fe particles could not sufficiently trap hydrogen due to the delay in diffusion at the interface (process (i)). It can be therefore inferred that, in HFeSi-HH material, hydrogen partitioning to the $MgZn_2$ precipitate and associated HE was suppressed only partially because the Al_7Cu_2Fe particles could not sufficiently trap hydrogen due to its slow diffusion through the particle interface and/or in the particle interior.

To fully employ the suppressive effect of Al_7Cu_2Fe particles on quasi-cleavage crack propagation, the time required for sufficient diffusion into the particle interior must be shortened, which can be achieved by reducing the size of the particles. In addition, reducing the size of the particles is effective even when hydrogen diffusion in the particle interior is extremely slow. In this case, as shown in Fig. 11(b), the trapped hydrogen in the particles is just below the surface of the particles. The total hydrogen concentration in the particles increases with increasing the surface area of the particles. Therefore, suppression of HE crack propagation by adding the Al_7Cu_2Fe particles appears to become more effective by reducing the particle size. In summary, it can be expected that HE can be suppressed in a material in which there is a fine distribution of small particles.

To discuss and confirm the quantitative HE suppressing effect of particles such as Al_7Cu_2Fe, which has high hydrogen trapping energy, it is necessary to study quantitatively the hydrogen diffusion behavior both in the interior of and at the interface of the particles, since there are no existing reports on hydrogen diffusivity in IMC particles.

5. Conclusion

In the present study, 4D HE behavior in two Al–Zn–Mg alloys with different hydrogen and IMC particle contents was observed. To investigate the specific conditions of a method for HE suppression, the influence of the Al_7Cu_2Fe particles on the local HE crack initiation and propagation behavior was evaluated. The following conclusions were obtained.

(1) The applied strain at which quasi-cleavage cracks initiate decreased with increasing hydrogen concentration, resulting in loss of ductility. The quasi-cleavage cracks initiated in a local region in which the Al_7Cu_2Fe particles are sparsely distributed. This is because the effect of suppressing hydrogen partition to the $MgZn_2$ precipitate interface was less effective.

(2) Even at high hydrogen concentrations, hydrogen partition to the $MgZn_2$ precipitate interface was suppressed due to the higher volume fraction of the Al_7Cu_2Fe particles. However, the highest fractional area of quasi-cleavage fracture was observed in HFeSi-HH material. Hydrogen partitioning to the $MgZn_2$ precipitate and associated HE are minorly suppressed because the Al_7Cu_2Fe particles could not sufficiently trap hydrogen due to its slow diffusion through the particle interface and/or in the particle interior.

(3) To summarize the effects of the distribution and size of Al_7Cu_2Fe particles on the initiation and propagation of HE cracks, it appears that HE can be suppressed by a fine distribution of small Al_7Cu_2Fe particles. In future, analysis of the hydrogen diffusion behavior within the particles and at the interface between matrix and particles will be needed to develop HE suppression strategies.

Acknowledgements

This study was supported by the Japan Science and Technology Agency (JST) CREST Grant Number JPMJCR1995, Japan and JST under Collaborative Research Based on Industrial Demand, “Heterogeneous Structure Control: Toward Innovative Development of Metallic Structural Materials”, Grant Number JPMJSK1412, Japan. The synchrotron radiation experiments were performed at the BL20XU at SPring-8, with the approval of the Japan Synchrotron Radiation Research Institute (JASRI) (Proposal No. 2019A0076, 2020A1531). The study was also partially supported by JSPS KAKENHI Grant Number JP20J11740 and 21K14037. The authors would also like to thank Mr. Masashi Ikemi for his contribution to the experimental parts.

REFERENCES

1) S. Lynch: Corros. Rev. **30** (2012) 105–123.
2) I.M. Robertson, P. Sofronis, A. Nagao, M.L. Martin, S. Wang, D.W. Gross and K.E. Nygren: Metall. Mater. Trans. A **46** (2015) 2323–2341.
3) J. Albrecht, A.W. Thompson and I.M. Bernstein: Metall. Trans. A **10** (1979) 1759–1766.
4) L. Christodoulou and H. Flower: Acta Metall. **28** (1980) 481–487.
5) N.D. Alexopoulos, C.J. Dalakouras, P. Skarvelis and S.K. Kourkoulis: Corros. Sci. **55** (2012) 289–300.
6) M.O. Speidel: Metall. Trans. A **6** (1975) 631–651.
7) A. Thakur, R. Raman and S.N. Malhotra: Mater. Chem. Phys. **101** (2007) 441–447.
8) K. Rajan, W. Wallace and J.C. Beddoes: J. Mater. Sci. **17** (1982) 2817–2824.
9) T. Ohnishi, Y. Ibaraki and T. Ito: Mater. Trans. JIM **30** (1989) 601–607.
10) T. Ohnishi and H. Kume: J. JILM **41** (1991) 582–589.
11) M.S. Bhuiyan, Y. Tada, H. Toda, S. Hang, K. Uesugi, A. Takeuchi, N. Sakaguchi and Y. Watanabe: Int. J. Fract. **200** (2016) 13–29.
12) M.S. Bhuiyan, H. Toda, Z. Peng, S. Hang, K. Horikawa, K. Uesugi, A. Takeuchi, N. Sakaguchi and Y. Watanabe: Mater. Sci. Eng. A **655** (2016) 221–228.
13) T. Tsuru, K. Shimizu, M. Yamaguchi, M. Itakura, K. Ebihara, A. Bendo, K. Matsuda and H. Toda: Sci. Rep. **10** (2020) 1998.
14) R. Oriani: Acta Metall. **18** (1970) 147–157.
15) S.W. Smith and J.R. Scully: Metall. Mater. Trans. A **31** (2000) 179–193.
16) K. Shimizu, H. Toda, H. Fujihara, K. Hirayama, K. Uesugi and A. Takeuchi: Eng. Fract. Mech. **216** (2019) 106503.
17) R. Ayer, J.Y. Koo, J.W. Steeds and B.K. Park: Metall. Trans. A **16** (1985) 1925–1936.
18) L.L. Liu, Q.L. Pan, X.D. Wang and S.W. Xiong: J. Alloy. Compd. **735** (2018) 261–276.
19) M. Yamaguchi, T. Tsuru, K. Ebihara, M. Itakura, K. Matsuda, K. Shimizu and H. Toda: Mater. Trans. **61** (2020) 1907–1911.
20) H. Zhao, P. Chakraborty, D. Ponge, T. Hickel, B. Sun, C.-H. Wu, B. Gault and D. Raabe: Nature **602** (2022) 437–441.
21) H. Su, H. Toda, K. Shimizu, K. Uesugi, A. Takeuchi and Y. Watanabe: Acta Mater. **176** (2019) 96–108.

22) C. Larignon, J. Alexis, E. Andrieu, L. Lacroix, G. Odemer and C. Blanc: Electrochim. Acta **110** (2013) 484–490.
23) K. Hirayama, H. Toda, D. Fu, R. Masunaga, H. Su, K. Shimizu, A. Takeuchi and M. Uesugi: Corros. Sci. **184** (2021) 109343.
24) Y. Wang, H. Toda, Y. Xu, K. Shimizu, K. Hirayama, H. Fujihara, A. Takeuchi and M. Uesugi: Acta Mater. **227** (2022) 117658.
25) R. Oikawa, K. Shimizu, Y. Kamada, H. Toda, H. Fujihara, M. Uesugi and A. Takeuchi: J. JILM **72** (2022) 411–419.
26) G.A. Young and J.R. Scully: Metall. Mater. Trans. A **33** (2002) 1167–1181.
27) W.E. Lorensen and H.E. Cline: ACM SIGGRAPH Comput. Graph. **21** (1987) 163–169.
28) M. Kobayashi, H. Toda, Y. Kawai, T. Ohgaki, K. Uesugi, D.S. Wilkinson, T. Kobayashi, Y. Aoki and M. Nakazawa: Acta Mater. **56** (2008) 2167–2181.
29) H. Toda, T. Hidaka, M. Kobayashi, K. Uesugi, A. Takeuchi and K. Horikawa: Acta Mater. **57** (2009) 2277–2290.
30) M. Yamaguchi, T. Tsuru, K. Ebihara and M. Itakura: J. JILM **68** (2018) 588–595.
31) M. Yamaguchi, M. Itakura, T. Tsuru and K. Ebihara: Mater. Trans. **62** (2021) 582–589.
32) T. Tsuru: unpublished work.
33) M. Yamaguchi, K. Ebihara, M. Itakura, T. Tsuru, K. Matsuda and H. Toda: Comput. Mater. Sci. **156** (2019) 368–375.
34) L. Ismer, M.S. Park, A. Janotti and C.G. Van de Walle: Phys. Rev. B **80** (2009) 184110.
35) T. Tsuru, M. Yamaguchi, K. Ebihara, M. Itakura, Y. Shiihara, K. Matsuda and H. Toda: Comput. Mater. Sci. **148** (2018) 301–306.
36) K. Shimizu, H. Toda, K. Hirayama, H. Fujihara, T. Tsuru, M. Yamaguchi, A. Bendo, K. Matsuda, M. Uesugi and A. Takeuchi: Acta Mater. (2022), under review.
37) M. Yamaguchi: in preparation.
38) Y. Xu, H. Toda, K. Shimizu, Y. Wang, B. Gault, W. Li, K. Hirayama, H. Fujihara, X. Jin, A. Takeuchi and M. Uesugi: Acta Mater. **236** (2022) 118110.
39) A. Bendo, K. Matsuda, S. Lee, K. Nishimura, H. Toda, K. Shimizu, T. Tsuru and M. Yamaguchi: Materialia **3** (2018) 50–56.
40) A. Bendo, K. Matsuda, S. Lee, K. Nishimura, N. Nunomura, H. Toda, M. Yamaguchi, T. Tsuru, K. Hirayama, K. Shimizu, H. Gao, K. Ebihara, M. Itakura, T. Yoshida and S. Murakami: J. Mater. Sci. **53** (2018) 4598–4611.
41) K. Shimizu, H. Toda, C. Kadogawa, H. Fujihara and A. Takeuchi: Materialia **11** (2020) 100667.
42) S. Osaki, J. Ikeda, K. Kinoshita and Y. Sasaki: J. JILM **56** (2006) 721–727.
43) P. Sofronis and R.M. McMeeking: J. Mech. Phys. Solids **37** (1989) 317–350.
44) H. Fujihara, H. Toda, K. Ebihara, M. Kobayashi, T. Mayama, K. Hirayama, K. Shimizu, M. Uesugi and A. Takeuchi: Acta Mater. (2022), under review.
45) S.L.I. Chan, H.L. Lee and J.R. Yang: Metall. Trans. A **22** (1991) 2579–2586.
46) H.G. Lee and J.-Y. Lee: *Perspectives in Hydrogen in Metals*, (Elsevier, 1986) pp. 421–426.
47) J.-L. Lee and J.-Y. Lee: Metall. Trans. A **17** (1986) 2183–2186.
48) J. Čermák, L. Král and B. David: Intermetallics **16** (2008) 508–517.
49) K. Katayama, H. Ushida, H. Matsuura, S. Fukada, M. Goto and S. Nakagawa: Fusion Sci. Technol. **68** (2015) 662–668.